Ionic wind produced by a DC needle-to-plate corona discharge with a gap of 15 mm

Etienne DEFOORT[1], Romain BELLANGER[1], Catherine BATIOT-DUPEYRAT[2], Eric MOREAU[1]∗

[1]University of Poitiers, Pprime institute, CNRS, ISAE-ENSMA, Téléport 2,

BP 30179, 86962 Futuroscope, France

[2]University of Poitiers, IC2MP, CNRS, 4 Rue Michel Brunet, 86000 Poitiers, France

∗ corresponding author : eric.moreau@univ-poitiers.fr

Abstract

The goal of the present study is to better understand the electrohydrodynamic phenomena occurring in 15-mm gap point-to-plate corona discharges supplied by positive and negative DC voltages, and to link them to the discharge regime. For that, discharge current measurements have been conducted and a 20 kHz Particle Image Velocimetry system has been used to characterize the ionic wind produced by the discharges. The main results are as follows: (a) the Townsend's law can always correctly interpolate the experimental I-V characteristics of a negative corona, even in presence of Trichel pulses, (b) in the case of a positive streamer discharge, the current does not follow the Townsend's law as it evolves in V^k with k = 4 in the present study, (c) Indeed, the discharge current becomes higher than the Townsend's law when the glow-to-streamer regime transition occurs, (d) the ionic wind is unsteady, more especially in the case of a positive corona for which it seems that its velocity is pulsed at the same frequency than the streamer one, (e) when the positive high voltage is switched on, a strong streamer occurs at the end of the voltage rising (t = 25 µs for +6 kV), resulting in an over-velocity region upstream the head of the ionic wind jet that progresses in quiescent air toward the plate, (f) the topology of the time-averaged ionic wind is fully different compared to the one observed in a previous study where the gap was equal to 25 mm, (g) in the case of a negative corona, the ionic wind velocity is nearly

constant in the electrode gap, (h) in the case of the positive corona, the results are even more surprising since the velocity is minimum at the tip and increases when one approaches the grounded plate, indicating that there is a significant space charge remained by the streamers in the second half of the inter-electrode region, (i) generally speaking, this study highlights that the spatio-temporal characteristics of the EHD force and the resulting ionic wind depend on the distribution of the space charge between both electrodes, the latter being linked to the voltage polarity, the discharge regime and the electrode gap.

I. Introduction

Although corona discharges in atmospheric air involve complex electrical, chemical and mechanical phenomena, they are easy to enforce. Therefore, they are used in numerous engineering applications, such as ozone production[1,2], reduction of gaseous pollutants[3,4], surface treatment[5], electrostatic precipitation[6–8] and more recently thrust production[9–11] for instance. Indeed, when a high potential difference is applied at a thin electrode (such as a needle or a wire), air molecules are ionized and a corona discharge is induced. Due to the electric field, the produced ions are submitted to Coulomb force, resulting in their motion from the high voltage electrode toward the grounded collecting one. The set of all these Coulomb forces results in a volume electrohydrodynamic (EHD) force occurring inside the discharge. Hence, in the electrode gap, many collisions between ions in motion and neutral air molecules take place, resulting in a momentum transfer that produces a gas flow, which is usually called "ionic wind". The first publication dedicated to this subject is the one of Chattok[12] in 1899, but we can say that theory of EHD in gas (also called EAD for electro-aerodynamics) started with the well-known publication of Robinson[13] in 1961 that investigated the ability of corona discharges to perfect blowers in absence of any moving mechanical part. More recently, for about 15 years, several others research groups have been studying corona discharges, with the aim at increasing the ionic wind velocity, the resulting flow rate and the electromechanical efficiency of such devices[14–24].

Recently, we investigated the ionic wind produced by negative and positive corona discharges ignited between a needle and a plate spaced by 25 mm[25,26]. In these both papers, interesting features were highlighted. First, we demonstrated that, in the case of a positive corona, the I-V curve did not follow the Townsend's law anymore when the glow-to-streamer regime transition occurred. However, we did not know if this feature was due to the high gap (25 mm) that resulted in energetic current pulses composed of several

successive streamers or not. Secondly, in ref. 25, we showed that the topology of the produced ionic wind is different according to the high voltage. Indeed, although the velocity is usually maximum around the tip, in the case of a positive corona in streamer regime, the velocity could be constant between both electrodes. One more time, because this feature had never been observed before our study, we could not know if it was specific to our experiments or if it could be verified at a smaller gap.

Consequently, the present paper aims at characterizing the ionic wind produced by a similar electrode geometry (point-to-plate) but with a smaller gap (equal here to 15 mm) and to link its properties to the discharge regime, the goal being to confirm or contradict our previous results. We will see in this paper that even if the electrical behaviour is close to the one observed with a 25-mm gap, the electrohydrodynamic phenomena and more particularly the ionic wind topology are entirely different.

II. Experimental Setup

In this study, we aim at characterizing the electrical and mechanical properties of positive and negative point-to-plane corona discharges. Thus, the high voltage V is applied between a tip and a grounded plane electrode. The tip is made of tungsten and has a curvature radius of about 100 µm when the grounded electrode is a stainless steel disk, which is 80 mm in diameter. These both electrodes are separated by a gap of 15 mm. As shown on Fig. 1, the needle is in a horizontal position and the plate electrode is placed perpendicularly to the needle. The needle is connected to a high voltage amplifier (Trek 30kV/40mA, slew rate equal to 600 V/µs) amplifying a low DC voltage supplied by a signal generator (Lecroy WaveStation 3082). The discharge current versus time i(t) is deduced from the measurement of the voltage across a 1 kΩ resistor connected between the plate and earth with a voltage probe (Lecroy PP018, 500MHz, 10 pF). All the signals are recorded with

a digital oscilloscope (Lecroy HDO6054, 500 MHz, 2.5 GS/s). For the time-averaged value of the discharge current I, which will be used to plot the I-V characteristics, two manners are employed. The first one consists in computing the time-averaged value from the measurements of i(t) with the oscilloscope, with a sufficient sampling frequency. The second type of measurements is carried out with an ammeter (model MAS-830, range 0-200 µA, precision around 1 µA). This method is cheaper but as we will see below, the measured value can be incorrect in certain conditions.

To characterize the ionic wind produced by the discharge, a LaVision time-resolved particle imaging velocimetry (PIV) system is used. The point-to-plane design is put into a PMMA tank ($30 \times 80 \times 40\,cm^3$). The air is seeded with dielectric oil droplets (Ondina 915) having a mean diameter equal to 0.3 µm. The light used to illuminate the seeding particles is produced by a 532 nm Nd-YAG laser generator (Continuum Mesa). PIV field images were acquired with a 20 kHz camera (Photron Fastcam SA-Z) so the time between two successive images is equal to 50 µs. The system is operated from a computer with LaVision DaVis software, which also gathers the experimental data. The resulting images have a resolution of 1024 x 1024 px^2, a size of 16.5 x 16.5 mm^2. 2000 images are recorded for every measure. The velocity is computed using a cross-correlation algorithm with adaptive multi-passes (LaVision DaVis software), with interrogation windows of 64 × 64 down to 16 × 16 pixels and an overlap set to 50%, leading to a final flow field resolution of one vector every 130 µm (or 7.7 vectors/mm).

Of course, measurements with a PIV system that requires seeding particles can be criticized because it can be suspected that their motion is not due to ionic wind but to electrostatic precipitation. In our case, as demonstrated in previous papers[25,26], we can affirm that particle motion is mainly due to ionic wind, for two reasons. First, after

experiments, there was no oil deposition on the grounded electrode. Secondly, in the case of electrostatic precipitation, particles follow the electric field streamlines and then they impact the grounded electrode perpendicularly. In our case, two vortices are well visible on both sides of the ionic wind jet, confirming that particles follow the flow streamlines and not the electric field ones.

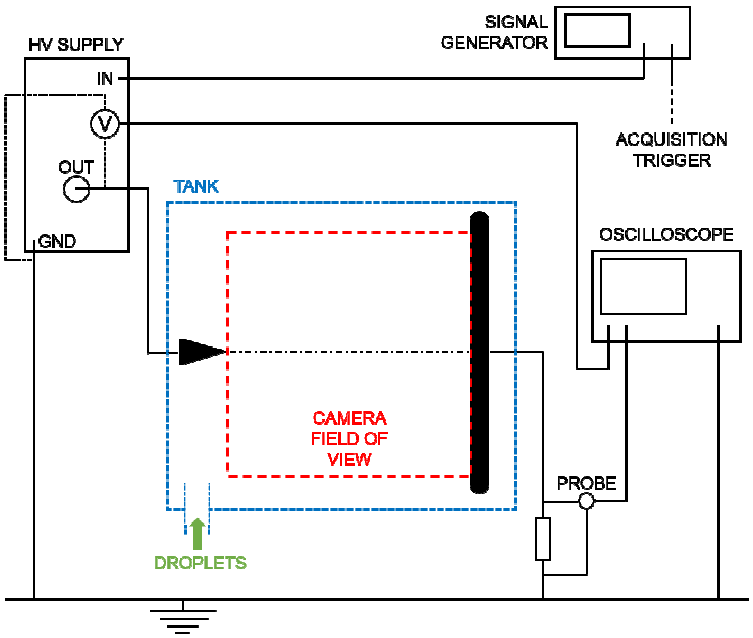

Figure 1. Experimental setup.

III. Electrical characteristics

In this part, we present the time-resolved and time-averaged discharge currents in a voltage range V from 4 kV up to 12 kV. Fig. 2 presents a typical example of the discharge current versus time for both positive and negative discharges (- 8 kV and + 8 kV). In the case

of a positive discharge (Fig. 2a), the current is composed of a dc component of about +10 µA (not visible on this figure because the scale is in mA) plus a pulsed positive current. As in ref 26, each pulse corresponds certainly to the propagation of several successive streamers in a branching process as the pulse duration is equal to about 400 ns when the time needed to one single streamer to cross the electrode gap is smaller than 100 ns. More precisely, from a voltage V = +4 kV and up to +6 kV, the discharge current is constant, without current pulses or only some erratic ones (not shown here). The discharge regime is then a glow (or corona) one. From +6 kV, streamer regime starts to occur, resulting in regular current pulses with a magnitude of 1 mA, 2 mA and 4 mA at V = +6 kV, +8 kV and +10 kV, respectively. The streamer frequency is around 5 kHz at +8 kV and it increases lightly with V. Compared to our previous results[26] with a gap of 25 mm, the voltage range for which the discharge regime is glow-type is more limited with a small gap, and the streamer regime is favored.

In the case of a negative voltage, Trichel pulses starts to appear from -6 kV, the current versus time being constant for smaller V values. Then the current is composed of a negative dc component plus Trichel pulses, the frequency of these pulses increasing with the HV value since their magnitude is rather constant (about 0.35 mA). At 8 kV (Fig. 2b), the Trichel pulse frequency is close to 190 kHz, this being in agreement with previous studies[19,27–29].

Let us now look at the I-V curves (Fig. 3a), while keeping in mind that the measurements are carried out in two ways (oscilloscope and ammeter). Several remarks can be done. First, we can see that the ignition voltage is about 4 kV, whatever the HV polarity is. In the case of the negative corona, the measured current values (red circles ●) does not depend on the measuring system and the experimental data can be well-interpolated by the Townsend's law (red solid curve) :

$$I = C \times V\,(V - V_0)$$

where V is the applied DC voltage, V_0 the ignition voltage value and C a constant depending on the electrode configuration, temperature, pressure and gas composition. In the case of a positive corona, the measured current value depends on the measuring system. On one hand, with the multimeter MAS-830 which does not take into account the pulsed component of the discharge current because its bandwidth is too low, the measured points (black squares, ■) can be well-interpolated by the Townsend's equation (black solid curve). On the other hand, with the high bandwidth oscilloscope, the pulsed component of the current is taken into account and the time-averaged current (open squares □) increases when the glow-to-streamer regime transition occurs. Then the measured current become greater than theoretical values and it can then be fitted by another expression:

$$I = C^* \times V^k$$

with C* a constant different than C and k = 4 in our case. This curve corresponds to the black dot line in Fig. 3a. This feature is interesting because it highlights one more time that the Townsend's equation is always appropriated in the case of a negative corona since it is not relevant in the case of a positive streamer corona discharge. Moreover, this feature has been observed by another research team in 2018 with a positive corona discharge in similar conditions with an electrode gap equal to 20 mm[30], confirming that the Townsend's law under-estimates the discharge current when the glow-to-streamer regime transition occurs, and this whatever the gap is between 15 and 25 mm.

Finally, Fig. 3b presents the electrical power consumption of both negative and positive coronas versus voltage, this power corresponding to the time-averaged value of V multiplied by i(t) computed with the oscilloscope. First, one can see that the power is weak (typically smaller than 0.5 W) and it is lightly higher with the negative corona, excepted for voltages

higher than ±11 kV. Moreover, logically, the power consumed by the negative and positive coronas can be fitted by the following expressions, respectively:

$$P = C \times V^2 (V - V_0)$$

$$P = C^* \times V^{(k+1)}$$

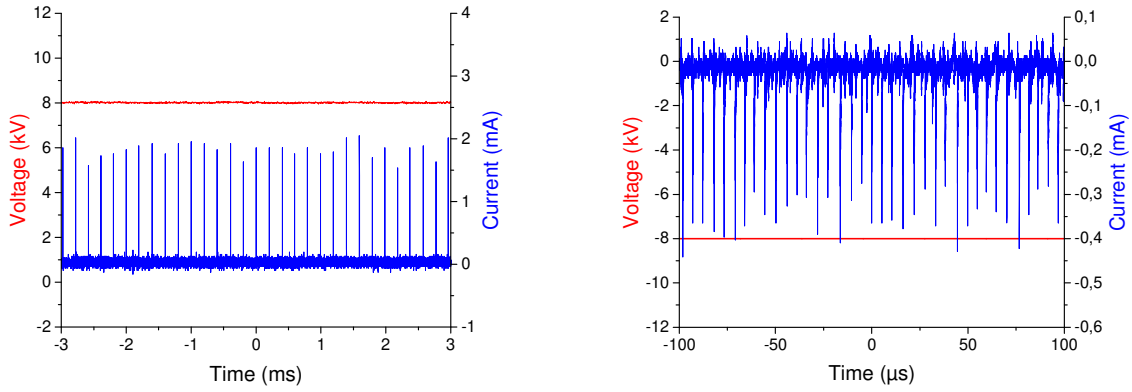

(a) (b)

Figure 2. Discharge current versus time for V equal to +8 kV (a) and -8 kV (b).

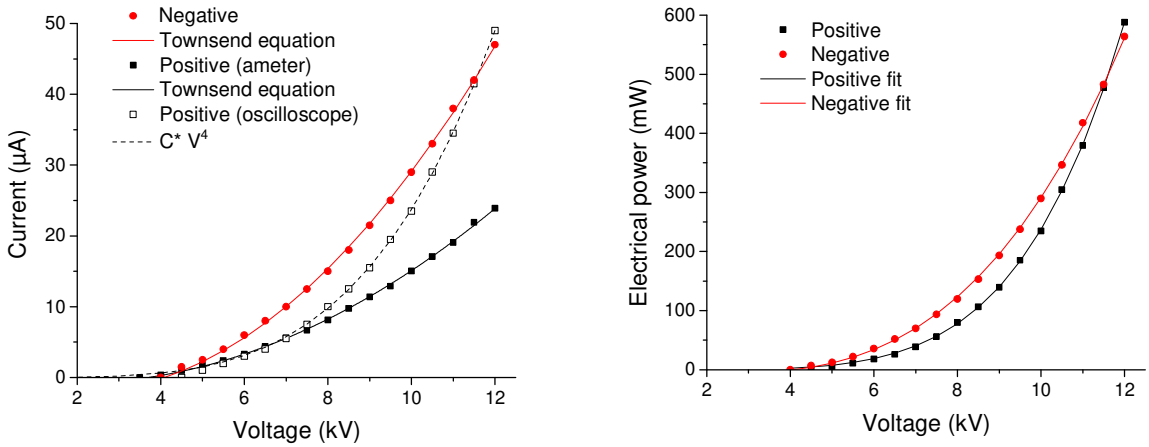

(a) (b)

Figure 3. Current-voltage characteristics for both positive and negative corona discharges (a) and electrical power consumption versus voltage (b).

IV. Characterization of the produced ionic wind by PIV

First, we aim at characterizing the time-resolved EHD flow when the discharge is switched on. The time-averaged velocity of gas when the ionic wind jet reaches its steady

state will be presented later. Fig. 4 presents the results for +6 kV and -6 kV, at different instants (t = 2, 4, 6, 8 and 12 ms, the high voltage being switched on at t = 0 with a slew rate of 600 V/µs *i.e.* 10 µs are needed to increase from 0 to 6 kV). The left and middle columns present the instantaneous velocity fields for the positive and negative coronas, respectively. Here, the needle is located at x = 0 and y = 0 when the plane electrode is located at x = 15 mm. Moreover, on the right, we plotted the profiles of the horizontal velocity component versus x, in front of the needle at y = 0. These figures allow us to observe the temporal evolution of the ionic wind topology at the moment when the discharge starts to occur.

First, in the case of a positive corona (Fig. 4a), a thin jet starts from the needle and it progresses rapidly in quiescent air toward the plane electrode. It reaches it in 6.5 ms, resulting in a wall-impinging jet with two vortices that rotates in opposite directions. This underlines that a three-dimensional axisymmetric annular vortex is developing against the wall. Secondly, we can observe that the velocity profiles present lots of peaks, highlighting that the ionic wind velocity is very fluctuating (Fig. 4c). Finally, we can see that the maximum velocity is not measured around the needle but it is always located at the jet head; at t = 4 ms, a region in which the velocity is strongly higher is visible at $7.5 \leq x \leq 9$ mm, at $10 \leq x \leq 13$ mm for t = 6 ms and finally at $10 \leq x \leq 14$ mm for t = 8 ms and 12 ms. This is even more visible on the velocity profiles of the right column (Fig. 4c), where we can see clearly a over-velocity at the jet head (shown by a pink narrow) followed downstream by a region of low velocity. For instance, at t = 4 ms, the over-velocity is around 4 m/s ($7.5 \leq x \leq 9$ mm) when the region of under-velocity (velocity of about 1 m/s) is located for x around 7 mm. Moreover, there is another over-velocity region; the latter is weaker than the first one (velocity $\approx$ 0.5 m/s) and takes place upstream the jet head (around x = 7 mm at t = 2 ms and

x = 11 mm at t = 4 ms, see blue narrow in Fig. 4c). These both features are surprising and interesting because they differs from what we measured with a 25mm gap in our previous study[25]. However, we will come back to this point below, in the discussion.

In the case of a negative corona, the ionic wind jet is different. On one hand, it is wider and slower (it reaches the plate in 10 ms instead of 6.5 ms) and there is no significant over-velocity region. On the other hand, and this differs from the results obtained with a 25-mm gap[25], the horizontal velocity profiles of the right column show that the velocity of the negative ionic wind velocity is very fluctuating, as for the positive ionic wind. In fact, if we do not take into account the two over-velocity regions located at the jet head in the case of a positive corona, the two profiles are very similar when the electrode gap is equal to 15 mm. This is certainly due to the presence of Trichel pulses as Mizeraczyk et al[31] highlighted recently that Trichel pulses play a key role in the dynamics of negative corona discharges.

In order to further study these velocity fluctuations, Fig. 5 shows the ionic wind velocity u(t) versus time. In Fig. 5a, we can see u(t) at x = 5 mm for +6 kV and -6 kV, from t = 0 to 50 ms. It highlights that the velocity fluctuations are higher for the positive corona. Indeed, u(t) varies between 2 m/s and 3.5 m/s (ΔU = 1.5 m/s) for the positive corona since ΔU is limited to about 0.7 m/s for the negative one. In Fig. 5b, we plotted u(t) for V = +6 kV at x = 5 mm and 10 mm, for 30 ms $\leq$ t $\leq$ 40 ms in order to zoom the velocity peaks. It is clear that the velocity fluctuations are higher at x = 10 mm. If we count the number of peaks in 10 ms, it can be estimated between 40 and 60, depending on what is considered as a peak or not, with a mean value around 50 (this has been verified with several u(t) curves, at different voltages). Consequently, even if the occurrence of these velocity peaks is not very regular, it seems that the mean duration between two successive peaks is around 200 µs, corresponding to a frequency equal to 5 kHz.

To confirm the fact that the velocity is not constant in the electrode gap even when the jet has reached its steady state, Fig. 6 presents two instantaneous velocity fields at t = 100 ms. One more time, one can observe the presence of successive regions of under and over-velocities, more visible in the case of the positive corona, highlighting that the produced ionic wind jet is not constant. One more time, this point will be discussed below, in the last part of the paper.

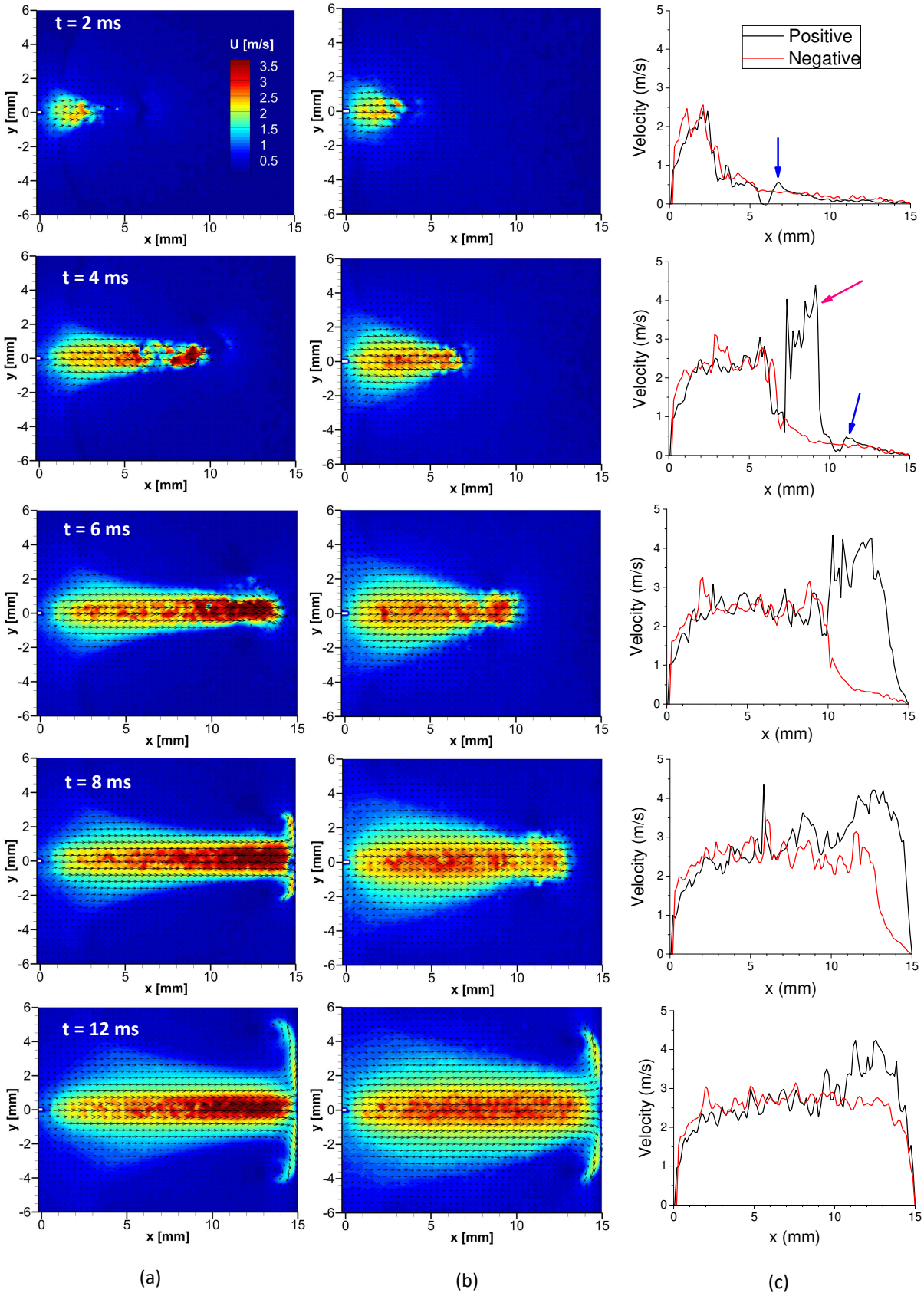

Figure 4. Instantaneous velocity vector fields for V = +6 kV (a) and V = -6 kV (b) and profiles of the horizontal velocity component versus x (at y = 0) at t = 2, 4, 6, 8 and 12 ms. The high voltage is switched on at t = 0. The color legend (corresponding to the velocity modulus) is indicated at the first field (t = 2 ms) of column (a).

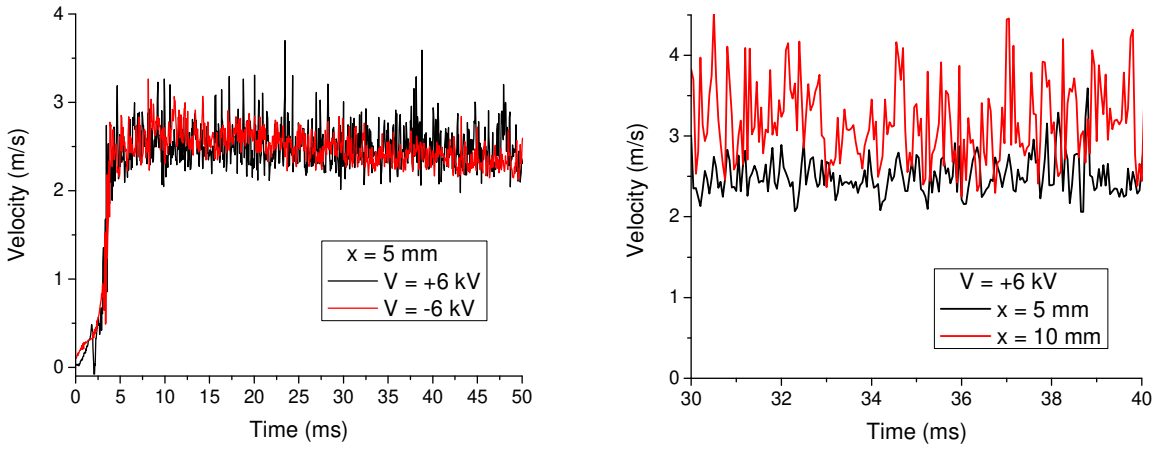

(a) (b)

Figure 5. Ionic wind velocity versus time at x = 5 mm for V = +6 kV and -6 kV from t = 0 to t = 50 ms (a), ionic wind velocity versus time for V = +6 kV at x = 5 mm and 10 mm for 30 ms ≤ t ≤ 40 ms (b).

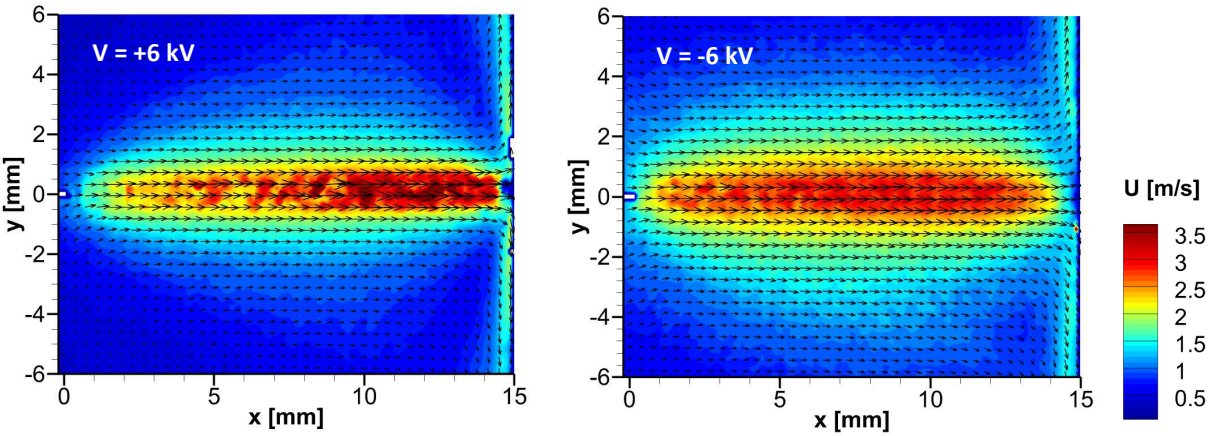

(a) (b)

Figure 6. Instantaneous velocity vector fields at t = 100 ms for V = +6 kV (a) and -6 kV (b).

After characterizing the temporal evolution of the produced ionic wind jet, we aim now at investigating its time-averaged behavior. Fig. 7 presents time-averaged velocity fields for positive and negative corona discharges, for applied voltages of ±6, ±7 and ±8 kV. For both polarities, a jet of a few mm in width is produced, and the ionic wind velocity increases with the applied voltage. However, there are some significant differences between both polarities, which are highlighted by Fig. 8 and 9.

In Fig. 8, which presents profiles of the horizontal component of the ionic wind velocity at x = 7.5 mm (midway between both electrodes), we can see that the velocity is always the highest in front of the needle, and it decreases when one moves away from this axis (located at y = 0). This result is well-known. However, it is surprising that the negative corona produces a higher velocity than the positive one since it is usually the opposite[15,25]. That said, the jet velocity depends on the x position. Fig. 9 presents profiles of the horizontal component of the ionic wind velocity along x (in front the needle, at y = 0), and we can see a very interesting feature, which is one more time fully different compared to the topology of the ionic wind measured with a larger electrode gap. Indeed, the maximum velocity is usually concentrated in a region close to the needle and this region grows and spreads progressively toward the plate when the high voltage is increased[25]. Then, the velocity decreases when moving toward the plate because the space charge, which is at the origin of the EHD force, is limited to a few millimeters around the tip. Consequently, when one moves away from the tip, the EHD force decreases and is not able to counter viscous effects.

In the present study, it is not the case. In the case of a negative corona, the velocity increases up to about x = 3 mm and then it is constant in the inter-electrode region before returning to zero at the wall, since the jet impacts the plate. In fact, there is a plateau for 3 mm $\leq$ x $\leq$ 12 mm. This feature means that the negative space charge at the origin of the EHD force is not concentrated only close to the point. Indeed, there is a sufficient EHD force in the electrode gap to counter viscous effects, resulting in a constant velocity in the whole inter-electrode gap. In the case of the positive corona, the velocity increases all along the x axis (from x = 2 mm to x = 13-14 mm), meaning that the EHD force is higher than viscous effects downstream this region. Moreover, if we look more closely, we can see that the slope of this curve increases from x $\approx$ 8 mm. This can be explained by the fact that there is a

specific positive space charge halfway between the two electrodes, inducing a higher EHD force at this location. We then ask ourselves the question of knowing the origin of this space charge. This point will be addressed in the following section.

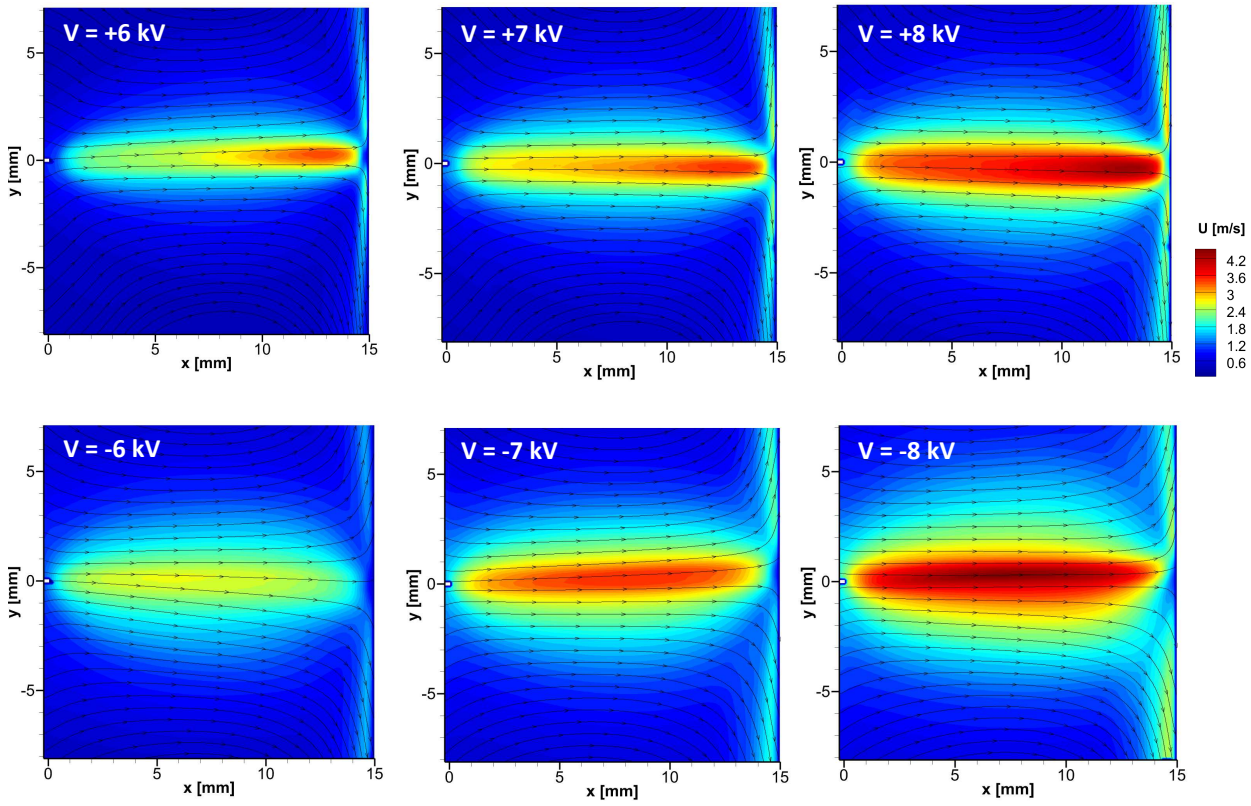

Fig. 7. Time-averaged velocity fields for positive and negative corona discharges, for applied voltages of ±6, ±7 and ±8 kV.

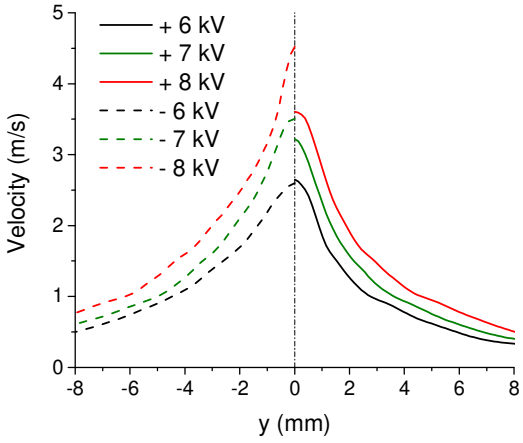

Fig. 8. Horizontal component of the ionic wind velocity at x = 7.5 mm. The right half-profiles for a positive corona (solid curves) and the left half-profiles for a negative corona (dot curves).

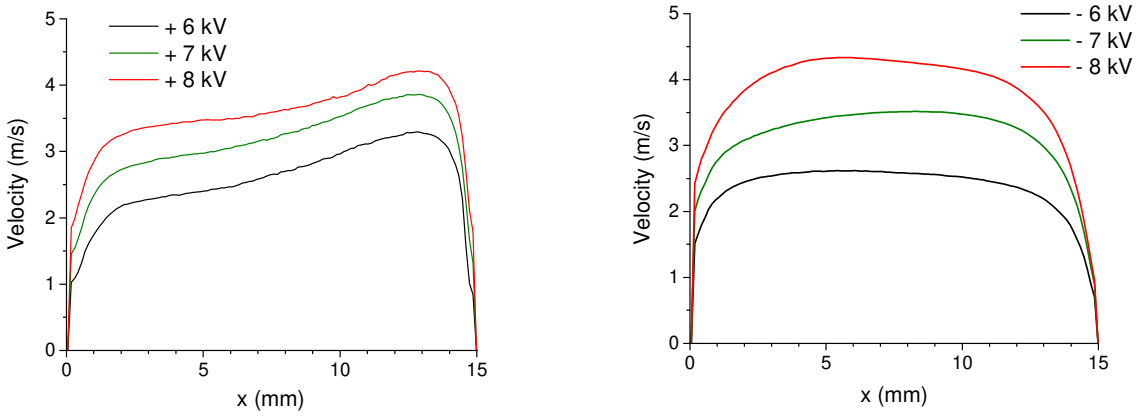

(a) (b)

Fig. 9. Horizontal component of the ionic wind velocity along x (in front the needle, at y = 0) in the case of a positive corona (a) and a negative corona (b).

VI. Discussion

As we highlighted, the ionic wind induced by corona discharges is always unsteady, whatever the applied voltage polarity is. However, this is even truer in the case of a positive corona. That means that the EHD force is not constant in time and in space. In fact, the spatio-temporal characteristics of the EHD force depend on the distribution of the space charge between both electrodes, the latter being linked to the voltage polarity and the discharge regime. Indeed, two recent studies highlighted that the electrohydrodynamics was linked to the streamer frequency in positive coronas[26] and the presence or not of Trichel pulses in negative coronas[31].

Let us focus on the case of the positive corona discharge. In ref. 26, we plotted the power spectra of both the current and the ionic wind velocity versus time with the help of a FFT computation, in the case of a 25-mm gap positive corona discharge. We showed that both spectra presented a peak at the same frequency, corresponding to the streamer frequency ($\approx$ 3.5 kHz). That meant that the ionic wind was pulsed at the same frequency than the streamer one. In this previous study, the voltage and the magnitude of the current peaks were higher ($\geq$ +16 kV, $\geq$ 4 mA) than in the experiments presented in the present article.

Thus the transferred charge and energy per pulse were higher too. Moreover, 3000 instantaneous velocity fields were available for the FFT computation. Unfortunately, in the present study, the space charge remaining after each current pulse is smaller and only 1500 samples are available (we cannot take into account the first 500 samples that correspond to the transient state). This is certainly the reason why although it seems that the velocity is pulsed at about 5 kHz (see Fig. 5b), the FFT spectrum does not present a clear peak at 5 kHz. This point is frustrating for us because it seems that the flow is pulsed at a frequency close to that of the streamers, but we cannot prove it by conventional processing methods.

Finally, let us comment the presence of the two over-velocity regions at the head of the jet when this one is ignited. First, there is a weak over-velocity region (velocity $\approx$ 0.5 m/s) that takes place upstream the jet head (around x = 7 mm at t = 2 ms and x = 11 mm at t = 4 ms, see blue narrow in Fig. 4c). Although this feature has ever been observed in previous studies in the case of a corona discharge[25] and a pulsed micro-discharge[32], it is surprising and its origin is not fully explained. To try to explain it, we observed the discharge current when the high voltage is just switched on, during the first microseconds (Fig. 10). This plot is interesting because it shows a strong current pulse of 7 mA at t = 25 µs (for V = +6 kV), corresponding to a first streamer that certainly remains a significant space charge at the origin of this weak over-velocity region (for comparison, the current peaks in steady state have a magnitude equal to about 1 mA at +6 kV). Furthermore, this assumption is confirmed by the fact that in absence of this first streamer (it is the case for the negative corona discharge), there is no over-velocity region.

The explanations concerning the second over-velocity region (see pink narrow in Fig. 4c) are more complicated. If we look at Fig 4a, we can see that it starts to appear at t = 4 ms, halfway between the two electrodes. In fact, if we look at more closely all the successive

velocity fields from t = 0 (not shown here because there is only 50 µs between two successive fields), we notice that this high over-velocity region starts to appear exactly at 3.8 ms et x ≈ 7 mm. Then it moves toward the grounded plate to be located between 10 mm and 14 mm for t = 6 ms. Moreover, this time-resolved behavior is confirmed by the time-averaged measurements of Fig. 9a that highlighted that the ionic wind velocity increases in the second half of the electrode gap. What could be the origin of this fluid acceleration in the second half of the inter-electrode region? Inevitably, the answer is a positive space charge. The second question is then: where does this space charge come from? This is only a hypothesis, but we think that it comes from the streamers. Indeed, after the first streamer occurring at t = 25 µs, several others streamers take place (see Fig. 2a), and we think that they remain a strong positive space charge in the second half of the inter-electrode region. As indicated above, it is a hypothesis and we are not able to demonstrate it definitively.

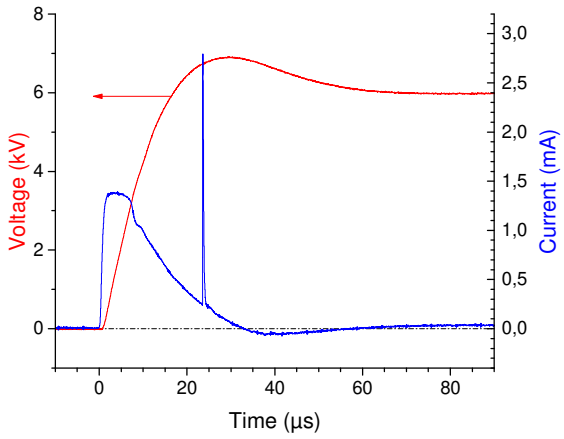

Fig. 10. Voltage and current in the first 90 µs (HV is switched on at t = 0).

VII. Conclusion

In this paper, we studied the ionic wind produced by positive and negative corona discharges and we tried to link its characteristics with the electrical properties of the discharge.

Concerning the electrical properties of a positive corona, we highlighted that the glow-to-streamer regime transition occurs at +6 kV, meaning that the current is composed of a dc component plus a pulsed one around 5 kHz. As a result, the total time-averaged discharge current increases compared to the Townsend's law and the I-V characteristic evolves as V^4. The reason why this phenomenon had never been observed before 2018[26,30] is certainly due to the fact that the current probes used in previous studies were not able to detect accurately the streamers and to take into account the pulsed component. For the negative corona, the Trichel pulses appear at -6 kV. However, even in presence of these Trichel pulses, the experimental I-V curve can be well fitted by the Townsend's law.

Concerning the analysis of the electroaerodynamic properties of the corona discharge investigated in the present paper, it shows that the resulting ionic wind is fully different compared to the one observed in ref. 25 for a gap equal to 25 mm.

On the one hand, the topology of the time-averaged ionic wind is not similar. For instance, in the case of a negative corona, the ionic wind velocity is nearly constant in the electrode gap at 15 mm since it was maximum close to the tip and decreased when one moved away from the tip at 25 mm. In the case of the positive corona, the results are even more surprising since the velocity is minimum at the tip and increases when one approaches the grounded plate, indicating that there is a significant space charge remained by the streamers in the second half of the inter-electrode region.

On the other hand, the characterization of the time-resolved ionic wind shows interesting features, more especially in the case of a positive corona. First, the fact that the ionic wind is pulsed at the same frequency than the one of the current pulses seems to be confirmed at 15 mm, highlighting the key role of streamers in the ionic wind dynamics. Secondly, we observed an over-velocity region at the head of the jet, certainly due to the space charge remained by a first streamer occurring, at the end of the rising time of the applied high voltage (t = 25 µs for V = +6 kV).

Finally, all these results highlight that the electroaerodynamic properties of a corona discharge depend strongly on the electrode gap. Consequently, it would be interesting and useful in a near future to precisely investigate the influence of the gap in a wide range, from 100 mm down to 1 mm for instance.

Acknowledgements

This work has been funded by the French Government program INVESTISSEMENT D'AVENIR (LABEX INTERACTIFS, reference ANR-11-LABX-0017-01).

References

1. Ono, R. & Oda, T. Dynamics of ozone and OH radicals generated by pulsed corona discharge in humid-air flow reactor measured by laser spectroscopy. *J. Appl. Phys.* **93**, 5876–5882 (2003).
2. Lukes, P., Clupek, M., Babicky, V., Janda, V. & Sunka, P. Generation of ozone by pulsed corona discharge over water surface in hybrid gas–liquid electrical discharge reactor. *J. Phys. Appl. Phys.* **38**, 409–416 (2005).
3. Masuda, S. & Nakao, H. Control of NO/sub x/ by positive and negative pulsed corona discharges. *IEEE Trans. Ind. Appl.* **26**, 374–383 (1990).
4. Kim, H. H., Takashima, K., Katsura, S. & Mizuno, A. Low-temperature NO $_x$ reduction processes using combined systems of pulsed corona discharge and catalysts. *J. Phys. Appl. Phys.* **34**, 604–613 (2001).
5. Ryu, J., Wakida, T. & Takagishi, T. Effect of Corona Discharge on the Surface of Wool and Its Application to Printing. *Text. Res. J.* **61**, 595–601 (1991).
6. Gilbert, L. A. & George, G. T. Electrical Resistance of Oxide Films formed on the Roll of a Corona Discharge Roll-Type Separator. *Nature* **194**, 1068–1069 (1962).
7. Dascalescu, L. *et al.* Charging of particulates in the corona field of roll-type electroseparators. *J. Phys. Appl. Phys.* **27**, 1242–1251 (1994).
8. Mizuno, A. Electrostatic precipitation. *IEEE Trans. Dielectr. Electr. Insul.* **7**, 615–624 (2000).
9. Christenson, E. A. & Moller, P. S. Ion-neutral propulsion in atmospheric media. *AIAA J.* **5**, 1768–1773 (1967).

10. Moreau, E., Benard, N., Lan-Sun-Luk, J.-D. & Chabriat, J.-P. Electrohydrodynamic force produced by a wire-to-cylinder dc corona discharge in air at atmospheric pressure. *J. Phys. Appl. Phys.* **46**, 475204 (2013).
11. Xu, H. *et al.* Flight of an aeroplane with solid-state propulsion. *Nature* **563**, 532–535 (2018).
12. Chattock, A. P. XLIV. *On the velocity and mass of the ions in the electric wind in air*. *Philos. Mag. Ser. 5* **48**, 401–420 (1899).
13. Robinson, M. Movement of air in the electric wind of the corona discharge. *Trans. Am. Inst. Electr. Eng. Part Commun. Electron.* **80**, 143–150 (1961).
14. Rickard, M., Dunn-Rankin, D., Weinberg, F. & Carleton, F. Maximizing ion-driven gas flows. *J. Electrost.* **64**, 368–376 (2006).
15. Moreau, E. & Touchard, G. Enhancing the mechanical efficiency of electric wind in corona discharges. *J. Electrost.* **66**, 39–44 (2008).
16. Tsubone, H. *et al.* Flow characteristics of dc wire-non-parallel plate electrohydrodynamic gas pumps. *J. Electrost.* **66**, 115–121 (2008).
17. Kim, C., Park, D., Noh, K. C. & Hwang, J. Velocity and energy conversion efficiency characteristics of ionic wind generator in a multistage configuration. *J. Electrost.* **68**, 36–41 (2010).
18. Colas, D. F., Ferret, A., Pai, D. Z., Lacoste, D. A. & Laux, C. O. Ionic wind generation by a wire-cylinder-plate corona discharge in air at atmospheric pressure. *J. Appl. Phys.* **108**, 103306 (2010).
19. Zouzou, N., Moreau, E. & Touchard, G. Précipitation électrostatique dans une configuration pointe-plan. *J. Electrost.* **64**, 537–542 (2006).
20. Moreau, E. Airflow control by non-thermal plasma actuators. *J. Phys. Appl. Phys.* **40**, 605–636 (2007).
21. Fylladitakis, E. D., Theodoridis, M. P. & Moronis, A. X. Review on the History, Research, and Applications of Electrohydrodynamics. *IEEE Trans. Plasma Sci.* **42**, 358–375 (2014).
22. Johnson, M. J. & Go, D. B. Recent advances in electrohydrodynamic pumps operated by ionic winds: a review. *Plasma Sources Sci. Technol.* **26**, 103002 (2017).

23. Jen-Shih Chang, Tsubone, H., Harvel, G. D. & Urashima, K. Narrow-Flow-Channel-Driven EHD Gas Pump for an Advanced Thermal Management of Microelectronics. *IEEE Trans. Ind. Appl.* **46**, 1151–1158 (2010).
24. Wang, C.-C. & Roy, S. Three-dimensional simulation of a microplasma pump. *J. Phys. Appl. Phys.* **42**, 185206 (2009).
25. Moreau, E., Audier, P. & Benard, N. Ionic wind produced by positive and negative corona discharges in air. *J. Electrost.* **93**, 85–96 (2018).
26. Moreau, E., Audier, P., Orriere, T. & Benard, N. Electrohydrodynamic gas flow in a positive corona discharge. *J. Appl. Phys.* **125**, 133303 (2019).
27. Trichel, G. W. The Mechanism of the Negative Point to Plane Corona Near Onset. *Phys. Rev.* **54**, 1078–1084 (1938).
28. Dordizadeh, P., Adamiak, K. & Castle, G. S. P. Experimental study of the characteristics of Trichel pulses in the needle-plane negative corona discharge in atmospheric air. *J. Electrost.* **88**, 49–54 (2017).
29. Berendt, A., Budnarowska, M. & Mizeraczyk, J. DC negative corona discharge characteristics in air flowing transversely and longitudinally through a needle-plate electrode gap. *J. Electrost.* **92**, 24–30 (2018).
30. Chen, S., van den Berg, R. G. W. & Nijdam, S. The effect of DC voltage polarity on ionic wind in ambient air for cooling purposes. *Plasma Sources Sci. Technol.* **27**, 055021 (2018).
31. Mizeraczyk, J., Berendt, A. & Podlinski, J. Temporal and spatial evolution of EHD particle flow onset in air in a needle-to-plate negative DC corona discharge. *J. Phys. Appl. Phys.* **49**, 205203 (2016).
32. Orrière, T., Moreau, É. & Pai, D. Z. Electric wind generation by nanosecond repetitively pulsed microplasmas. *J. Phys. Appl. Phys.* **52**, 464002 (2019).